Vessel segmentation for time resolved phase contrast MRI

Sebastian Bidhult

March 26, 2013

Abstract

Quantification of cardiovascular flow and blood volumes is a useful tool in diagnosing cardiovascular disease such as congenital heart defects and different kinds of valve leakage. Medical imaging techniques enables non-invasive analysis of anatomy and physiology. In order to perform flow quantification from medical image sequences, the boundaries of the vessels of interest are usually delineated manually by medical professionals. This is a time consuming process and the result depends, to a high degree, on user experience.

This thesis presents an automated vessel segmentation method for the main vessels around the heart from velocity encoded Magnetic Resonance Imaging sequences. The proposed method only require a manual delineation in one image. The algorithm is based on an active contour, using the Euler-Lagrange equation together with internal and external forces designed from a set of fundamental assumptions regarding vessel shape and behaviour. More specifically, constraints were applied to the geometrical shape and elasticity of a vessel. Validation of the method was performed by comparing the detected stroke volume with manual delineation, and also by measuring the segmentation overlapping of the two methods. On a test set of 20 patients, 19 resulted in excellent segmentation agreement with manual delineations, with a mean Dice coefficient over 0.8. However, performance instability was observed when changing the values of two algorithm parameters, and one of the patients in the set constantly resulted in segmentation failure for all tested parameter combinations. The relative variability in stroke volume between the proposed algorithm and manual delineation was, at best, $6\pm$ 3.6%. This is comparable to the interobserver variability from a previous physiological study [1] of $3 \pm 4\%$, which indicates the potential of the suggested method if improvements in robustness and stability is implemented.

Contents

Chapter 1

Introduction

The effectiveness, robustness and overall complexity of the circulatory system have fascinated scientists for centuries, and the fact that cardiovascular disease is the number one cause of death in the world [2] makes cardiovascular studies a prioritized field in clinical research.

Despite extensive research in the field, many aspects of the cardiovascular system are still subjects for debate in the research community. The pumping mechanism of the cardiac muscle and the intra-vascular fluid dynamics are two examples of such aspects. The limitations of using in-vitro, invasive measurements for physiological studies made conducting studies in cardiovascular research particularly difficult for many years. However, the function of the circulatory system can now be measured with in-vivo, non-invasive medical imaging techniques such as X-ray-Computed Tomography (CT), Single Photon Emission Computed Tomography (SPECT) and Magnetic Resonance Imaging (MRI).

One method to study the pumping mechanism of the heart is to quantify the blood-flow from MRI sequences of the surrounding vessels. Furthermore, quantitative flow analysis is an integral part of routine cardiovascular magnetic resonance examinations [3]. The acquired data features high temporal and spatial resolution, why flow calculations require a time consuming, manual delineation of the vessels containing the flow of interest. The alternative is to use automated, post-processing algorithms for vessel segmentation with minimal user input. However, in order to avoid the need for detailed inspection by the user, such methods have to feature reliable precision regardless of image quality and different patient pathologies.

This thesis suggests, and explores the potential of a vessel segmentation and tracking algorithm which use a shape preservation assumption, in combination with both anatomical (Magnitude) and velocity (Phase) information from Phase-Contrast MRI image sequences to delineate the main arteries and veins of the heart. The method is validated by comparing its delineations and calculated flow with the result of manual delineations done by medical expertise.

The thesis is part of a student project in the Lund Cardiac MR Group at Lund University Hospital, which consists of eleven physicians, five engineers/mathematicians, two research technical assistants and one physiotherapist. The algorithm is developed for use in the medical image analysis software package Segment, a cooperative effort between the Lund Cardiac MR Group and Medviso AB.

Chapter 2

Background

This chapter presents brief information of medical image acquisition techniques, basic anatomy and physiology of the cardiovascular system and the underlying mathematical theory used in this thesis. A reader familiar with the mentioned topics may omit this chapter.

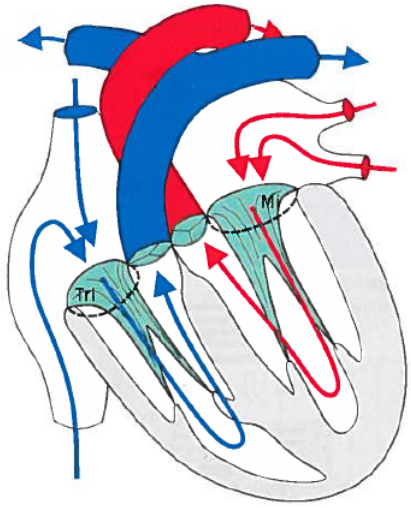

Figure 2.1: Illustration of the heart anatomy, Adopted from [4] with permission. The image shows the direction of bloodflow in the main arteries and veins of the heart. Blue arrows or vessels indicate deoxygenated blood while red arrows or vessels indicate oxygenated blood.

2.1 Physiology and anatomy of the circulatory system

The essential components of the circulatory system are blood, blood vessels and the heart. It is separated into two circuits, the **pulmonary circulation** (bloodflow to and from the lungs) and the **systemic circulation** (bloodflow through the rest of the body) which intersects at the heart. The function of the circulatory system is to ensure a continuous exchange

of oxygen, nutrients and metabolic end products between the blood and all other cells in the body. It also serves as one of the means of transport for antibodies of the immune system. An effective exchange requires a constant uni-directional flow of blood through the capillaries, a so called bulk flow, which occurs due to pressure changes produced by the pumping mechanism of the heart.

The heart is a muscle organ which is divided into two chamber pairs (left/right), where each pair consist of an upper chamber, the atrium, and a lower chamber, the ventricle. In a healthy human being blood is allowed to flow between the atrium and its corresponding ventricle through atrioventricular (AV) valves, while the two ventricles are separated by a muscular wall, the interventricular septum, which prevent any direct exchange of blood between the two compartments. Furthermore, in a healthy, normal heart no direct blood flow exist between the right and the left atria.

The anatomy of the heart and the surrounding blood vessels are illustrated in Figure 2.1. Deoxygenated blood from the **systemic circulation** enters the heart through **vena cava inferior** and **superior** into the right atrium, which empties in the right ventricle, where the blood is pumped into the **pulmonary circulation** through the **pulmonary artery**. The blood is oxygenated in the lungs and transported back to the heart through the **pulmonary veins** into the left atrium. The newly re-oxygenated blood is emptied into the left ventricle where it is finally pumped out to the **systemic circulation** through the **aorta**.

The pumping mechanism of the heart is controlled by coordinated nerve impulses which propagate across the heart in a predictable pattern. An impulse is initiated from the **sinoatrial** (SA) node, located near the entrance of the **superior vena cava**, from where it spreads down the atrium to the **atrioventricular** (AV) node, located at the base of the right atrium. The impulse finally propagates from the AV node down to the ventricles. The nerve impulse leads to an initial contraction of the muscle cells in both atria, followed by muscle contractions of both ventricles. The muscle cells of the heart is unable to sustain a contracted state for prolonged periods of time and requires a relatively long **absolute refractory period** of inactivity between contractions, a so called relaxation period. During the ventricular relaxation period the contraction of both atria start and the blood volumes of the ventricles are refilled. Atrial relaxation occurs at the same time as ventricular contraction, which together result in atrial filling. The periodic sequences of ventricular contraction and relaxation can be observed by ECG and blood pressure measurements. The ventricular contraction/atrial filling phase associated with high arterial blood pressure is called **systole**, while the ventricular filling/atrial contraction phase is called **diastole**. It is mainly the absolute refractory period, together with the coordinated nerve impulse propagation, that enables an effective blood-pumping mechanism. The nerve impulse coordination result in the sequential atrial/ventricle contractions (the pumping action), and the absolute refractory period enables relaxation of heart muscle.

The blood volume pumped from each ventricle per minute is defined as the **cardiac output**, which is the product of the **stroke volume** (pumped blood volume/heartbeat) times the **heart rate** (heartbeats/sec). The cardiac output indexed to body surface area is called cardiac index (CI). Furthermore, the volume fraction of blood pumped out of a ventricle in a heartbeat is called the ejection fraction (EF) and is defined as the stroke volume (SV) divided by the ventricular volume in the end of diastole (EDV). Blood flow analysis of the vessels surrounding the heart may reveal abnormal heart conditions and heart pathologies which impact blood volumes in and out of the heart. For example, abnormal blood outflow

ratios between the left and the right ventricle (QP/QS analysis) may originate from atrial or ventricular shunts, or from valve leakage, such as regurgitation or insufficiency

2.2 Medical image acquisition techniques

The rapid technological advancements of the twentieth century has paved the way for new, non-invasive, *in-vivo* imaging-techniques capable of depicting anatomy and physiology of the human body. One suitable method for studying the cardiovascular system is Phase Contrast Magnetic Resonance Imaging (PC-MRI), which have the ability to measure velocity. This technique enables time-resolved quantification of blood-flow.

2.2.1 Magnetic Resonance Imaging

MRI-imaging use the magnetic spin of charged particles to image human anatomy. Charged particle nuclei precess around its own axis with a so called Larmour frequency ω_0 which give rise to a magnetic moment of the particle. The Larmour frequency is proportional to the external magnetic field strength B_0 and the gyromagnetic ratio γ, a measure unique for each element (Eq. 2.1). When a human body is exposed to an external, homogeneous magnetic field, B_0 (Eq. 2.1), hydrogen nuclei starts to align themselves with the magnetic field and the sum of all aligned magnetic moments creates a net magnetization vector M_Z. The physical plane, for which M_Z is plane-normal, is called the xy-plane. The aligned nuclei precess out of phase and the great number of aligned, charged nuclei will result in a net magnetization of zero in the xy-plane. However, a radio pulse with a frequency identical to the Larmour frequency w_0 will make the nuclei precess in-synch which, in turn, creates a magnetic component in the xy-plane. When the radio pulse is stopped the nuclei return to out of phase precession. In this process of recovery, also called the relaxation period, the charged particles emits RF signals with frequency w_0, a signal which can be detected as an induced current in external magnetic coils. This signal is commonly referred to as the MRI signal.

$$\omega_0 = \gamma B_0 \tag{2.1}$$

In simplified terms, the MRI machine generates a strong, homogeneous, external magnetic field, sends out an RF-pulse, detects the returned MRI signal and finally creates an image with the same signal. Three gradient fields (G_Z, G_X, G_Y) are added to the external magnetic field which alters the Larmour frequency and phase of particles at different locations. This enables the MRI machine to distinguish MRI signals of varying spatial origin, and thus acquires the spatial resolution needed for image construction.

2.2.2 Phase-Contrast MRI

Phase Contrast Magnetic Resonance Imaging (PC-MRI) is a variation of conventional MRI which use the phase shift of the MRI signal from moving, charged particles to detect velocities inside the body. The phase shift $\Delta\phi$ associated with a uniform particle motion is proportional to the velocity v, the gyromagnetic ratio γ and the time integral of the magnetic field gradient $G(r,t)$ (Eq. 2.2)[5]. PC-MRI applies two consecutive gradients with different field strengths G_1, G_2 to dephase and rephase the charged particles in the direction of interest, and thus obtaining the expression in (Eq. 2.3). Since all terms are known except v, the velocity can be estimated [6].

$$\Delta\phi = \gamma v \int_0^T G(r,t)dt = \gamma v \hat{G} \tag{2.2}$$

$$\Delta\phi_1 - \Delta\phi_2 = \gamma v \cdot (\hat{G}_1 - \hat{G}_2) \tag{2.3}$$

The resulting "phase-image" is a mapping of velocities in the gradient pair direction, onto the MRI image plane. Additionally, PC-MRI measurements use the magnitude of the MRI signal to depict the anatomy in the MRI image plane, a so called magnitude image. A magnitude-phase image pair located slightly above the heart atria, in mid systole, is shown in Figure 2.2.

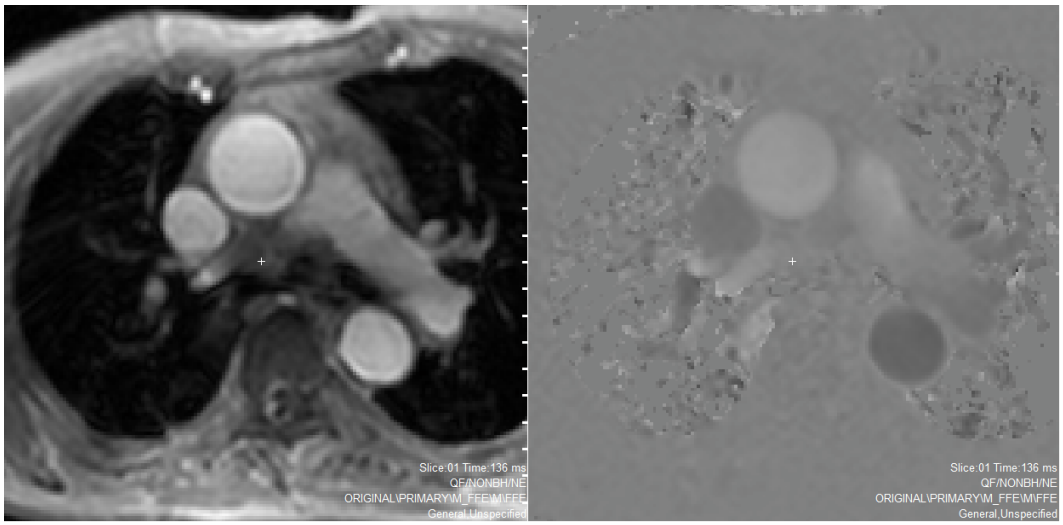

Figure 2.2: The magnitude image (left) and its corresponding phase image (right) from a PC-MRI scan. In the phase image, bright intensities represent high velocity in the gradient direction (perpendicular to the image plane) while dark intensities represent high velocity in the opposite direction.

2.3 Image data and clinical software

All clinical data used during development and testing of the proposed algorithm were taken from a previously conducted study of cardiac output/cardiac index by Carlsson, M, et al. [1]. In this study the, cardiac index was measured (by measuring aortic flow) in 144 healthy volunteers, 60 athletes and 157 patients with an ejection fraction (EF) below 40 percent. Aortic flow was measured with velocity encoded cardiac MRI (PC-MRI). In this thesis, 20 of the 157 patients were used in the validation process (see Section 4.3 for details).

2.3.1 Segment

Segment is an image analysis software package for analysing and manually interacting with multidimensional, medical image data. Segment was originally presented in [7]. It was developed in Matlab, by the Cardiac MR Group in collaboration with Medviso AB, and is distributed freely to the research community. The main features of Segment are:

- Tools for visualisation, ROI analysis, segmentation and manual measurements.
- All algorithms have been validated and published.
- Fully customizable source code version.
- FDA approved, commercial standalone version (FDA510k).
- Full support for DICOM files (vendor independent).
- Focused on cardiovascular MRI, but also support Cardiac CT and myocardial perfusion SPECT images.

A screenshot of the GUI for segmentation and ROI analysis can be found in Figure 2.3 The algorithm proposed in this thesis is based on a framework and code from previously implemented algorithms in Segment and the code is written as a plugin for the source code version of Segment v 1.9 R2760.

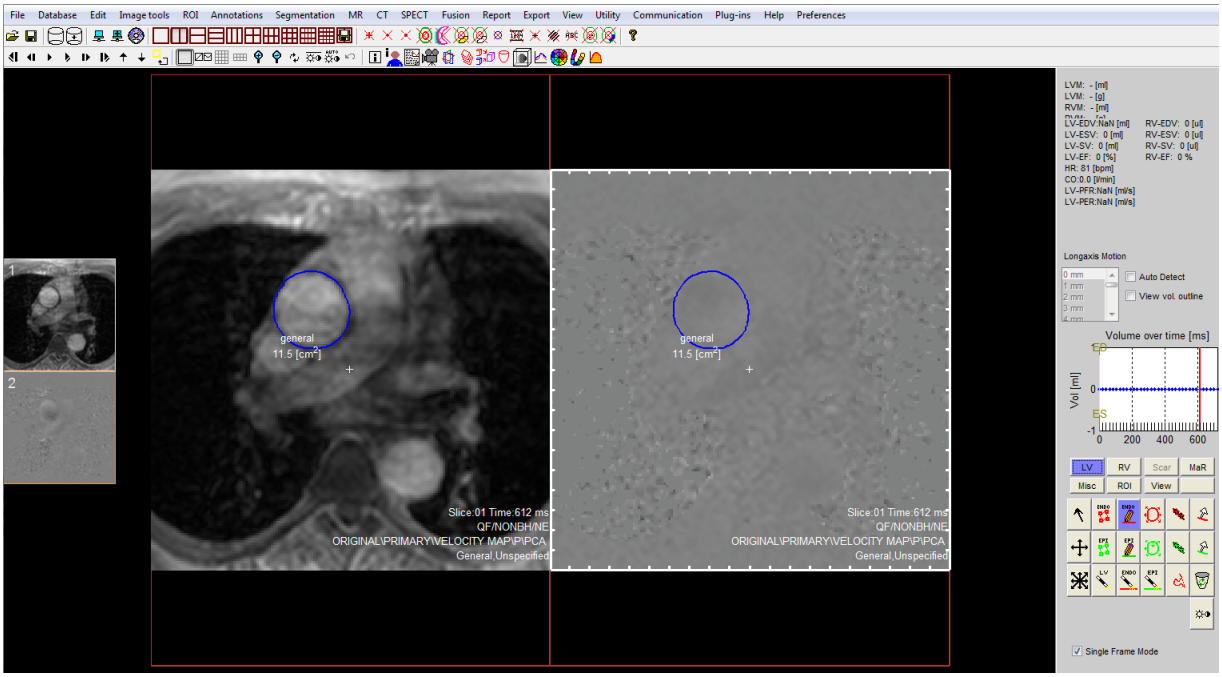

Figure 2.3: A screenshot of the main GUI of Segment.

2.4 Image processing

Image analysis is the theory of mathematical image interpretation. One application of image analysis is to extract interesting objects in an image through feature detection. Edges, corners and local intensity distributions are often used as features, and in most cases, some form of preprocessing is required for effective detection. The preprocessing stage often consist of image filtering/smoothing which brings out general shape trends in an image and filter out high frequency content to suppress noise in the final feature detection. The image is convolved with a two-dimensional filter kernel to produce the output. This process is highly dependent on the choice of filter kernel. A common smoothing kernel is the two-dimensional Gaussian filter, although the mean- and median filters are also used regularly. Many feature detection algorithms for edge and corner detection make use of two-dimensional differentiation filters, while local intensity-based methods mostly rely on analysis of regional statistics.

2.4.1 Edge detection

The purpose of edge detection is to identify intensity discontinuities in an image. The first and second order spatial derivatives are commonly used as discontinuity measures and the two most common approaches for edge detection are:

1. Laplacian methods: Examine stationary points of the first order derivatives, where the second order derivative is zero.

2. Gradient based methods: Use the magnitude of first order derivatives as a direct measure of discontinuity.

Both of these methods use image filters to detect edges but the choice of filter kernel sets them apart. Laplacian methods use a two-dimensional laplacian filter kernel, while gradient based methods use both first order derivatives of the x- and the y- direction. Of the two approaches, the gradient based method is often preferred since the laplacian filter is unoriented in space, and therefore do not posses the ability to distinguish longitudinal and horizontal edges. Both methods use two-dimensional convolution to produce the filter output.

2.4.2 Regional statistics

Statistic analysis in images have been used for many application, including (but not limited to): noise characterization, object classification and statistical pattern recognition. Object classification in images, where pixels with similar behaviour are grouped into one of K classes, is commonly formulated as a probabilistic problem. One approach is to view the image as a mixture of maximally separated Gaussian probability density functions (pdf), assign each class k to one of these functions, and finally assign the class, of which pdf result in the highest probability for pixel x, to x. One common algorithm to calculate such Gaussian mixtures is the EM algorithm [8].

2.5 Active Contours

A deformable model defines a closed contour in an image which is attracted to certain features and structures. The contour starts out as a delineation around the object/feature to be segmented and then deforms by a set of forces. The forces originates from both internal properties of the contour (curvature, shape etc.) and external properties such as edges,

regional intensity-statistics, etc. Deformable models are often used in medical image analysis for segmentation of moving objects such as heart ventricles and blood-vessels.

2.5.1 Definition

A gray-scale image I can be defined as an intensity mapping on a rectangular subset D of the plane:

$$D = [0, a] \times [0, b];\ D \subset R^2, \tag{2.4}$$
$$I : D \to [0, 1], \tag{2.5}$$
$$\mathbf{x} = (x, y) \in D;\ \ I(\mathbf{x}) = I(x, y) \in [0, 1]. \tag{2.6}$$

$\mathbf{x}$ represents a pixel in the image plane D and $I(\mathbf{x})$ is the gray-level intensity at the pixel $\mathbf{x} = (x, y)$. The active contour is defined as a parametrized, closed curve:

$$\gamma : [0, 2\pi] \to D \subset R^2 \tag{2.7}$$
$$\gamma_l(s) \subset D,\ 0 \leqslant s \leqslant 2\pi \tag{2.8}$$

The subscript l stands for the iteration in which γ_l represents the contour. Two central concepts that have to be understood in order to effectively use a deformable model are:

1. The curve representation in D.
2. The mechanism behind the curve evolution.

The curve evolution is driven by both internal and external deformation forces and the representation of the curve in the image can be formulated in a variety of ways, although the two most common representations are the finite difference- and the finite element method.

2.5.2 Curve representation

The finite difference method

The contour is represented as a set of discrete nodes in the image and continuous differentiation is approximated by finite differences. An accurate approximation requires small node-distances to prevent significant loss of information in the node-gaps. However, too small distances between nodes might give rise to behavioural loops and instabilities in the curve evolution [9].

The finite element method

To circumvent the problems associated with a strictly discrete curve-representation, the finite element method uses piecewise-polynomial interpolation between nodes to form a continuous contour [9]. This eliminates the node-gap problem, since the contour is explicitly known everywhere. The required number of nodes to represent a curve is also considerably less with the finite element method, compared to the finite difference method. Furthermore, the finite element method results in an increased computation speed and improved stability, but requires equidistant node resampling when neighbouring nodes get too close.

2.5.3 Deformation mechanism

The contour deformation is, much like most processes in nature, driven by an energy minimization mechanism which strive to keep the energy of the contour as low as possible. The energy gradient along the curve controls the magnitude and direction of the deformation force, which in turn give rise to the curve evolution. The total energy of the contour E is formulated as the integral of the local energy potential P at a certain point on the curve. The potential P can be divided into one internal and one external component. The internal potential originates from the properties of the curve itself, such as the local shape and curvature, while the external potential is generated by local image properties at the current curve position s. Minimizing the energy of the entire contour involves minimization of the curve integrals for both internal and external potentials:

$$E : D \rightarrow R \tag{2.9}$$

$$E(\gamma_t) = \int_0^{2\pi} (P(\gamma_t(s)))ds = \int_0^{2\pi} (P_{Int}(\gamma_t(s)) + P_{Ext}(\gamma_t(s)))ds; \tag{2.10}$$

If the net-energy potential P at a specified curve-point $\gamma_t(s)$ is assumed to vary with the coordinate $\gamma_t(s)$, the local curvature velocity $\frac{d\gamma_t(s)}{ds}$ and the current curve position s, the Euler-Lagrange differential equation can be applied to the the energy minimization problem. The existing minima is assumed to be a stationary point where $dE = 0$:

$$\gamma = \gamma_t(s) \tag{2.11}$$

$$\dot{\gamma} = \frac{d\gamma_t(s)}{ds} \tag{2.12}$$

$$P = P(\gamma, \dot{\gamma}, s) \tag{2.13}$$

$$E = \int_0^{2\pi} P(\gamma, \dot{\gamma}, s)ds \Rightarrow \tag{2.14}$$

$$dE = \int_0^{2\pi} (P(\gamma + \Delta\gamma, \dot{\gamma} + \Delta\dot{\gamma}, s) - P(\gamma, \dot{\gamma}, s))ds \tag{2.15}$$

$$= \int_0^{2\pi} (P + \frac{dP}{d\gamma}\Delta\gamma + \frac{dP}{d\dot{\gamma}}\dot{\Delta\gamma} + \mathcal{O}(\Delta\gamma^2) - P)ds = 0; \tag{2.16}$$

The second order terms are omitted since $\Delta\gamma^2 \approx 0$:

$$\dot{\Delta\gamma} = \frac{d(\Delta\gamma)}{ds}; \tag{2.17}$$

$$dE = \int_0^{2\pi} (\frac{dP}{d\gamma}\Delta\gamma + \frac{dP}{d\dot{\gamma}}\frac{d(\Delta\gamma)}{ds})ds \tag{2.18}$$

$$= \int_0^{2\pi} (\frac{dP}{d\gamma}\Delta\gamma + \frac{d}{ds}(\frac{dP}{d\dot{\gamma}}\Delta\gamma) - \frac{d}{ds}(\frac{dP}{d\dot{\gamma}})\Delta\gamma)ds \tag{2.19}$$

$$= \int_0^{2\pi} \Delta\gamma(\frac{dP}{d\gamma} - \frac{d}{ds}(\frac{dP}{d\dot{\gamma}}))ds + [\frac{dP}{d\dot{\gamma}}\Delta\gamma]_0^{2\pi} = 0 \tag{2.20}$$

The last term in the left hand side of (Eq. 2.20) is zero since $\Delta\gamma(0) = \Delta\gamma(2\pi) = 0$, by definition. Furthermore, $\Delta\gamma(s)$ for all other s are strictly not equal to zero. These assumptions

combined with the equation for dE gives the Euler-Lagrange differential equation:

$$dE = \int_0^{2\pi} \Delta\gamma(\frac{dP}{d\gamma} - \frac{d}{ds}(\frac{dP}{d\dot{\gamma}}))ds = 0 \Rightarrow \tag{2.21}$$

$$\frac{dP}{d\gamma} - \frac{d}{ds}(\frac{dP}{d\dot{\gamma}}) = 0 \tag{2.22}$$

This means that the Euler Lagrange differential equation must be satisfied at all stationary points of E. The right hand side of (Eq. 2.21) can be rewritten as a force balance equation of the form:

$$F_{ext} = \frac{dP}{d\gamma};\ F_{int} = -\frac{d}{ds}(\frac{dP}{d\dot{\gamma}}) \Rightarrow \tag{2.23}$$

$$F_{ext} + F_{int} = 0; \tag{2.24}$$

The external forces are formulated as the potential variation due to changes in curve coordinates, while the internal forces are the potential variation due to changes in local curvature.

Chapter 3

Aim

The aim of this thesis is to develop a reliable, automated method for vessel segmentation and tracking in PC-MRI images. The purpose of automated methods is to standardize the delineation methodology in order to make the delineation quality less dependent on individual user experience, narrow the performance gap between experienced and inexperienced individuals, and to ease the workload for all users.

More specifically, the thesis aims to:

- Develop an automated vessel segmentation and tracking algorithm based on a set of fundamental assumptions regarding the nature of vessel shape and behaviour in PC-MRI data.
- Validate the suggested method by comparison with manual delineation (gold standard) in a test set consisting of 20 patients.

Chapter 4

Method

The deformable model for vessel tracking and segmentation use the basic framework from a previously developed segmentation algorithm [10]. Both methods share the same curve representation and use the same assumptions for the Euler-Lagrange force equilibrium equation. However, The two algorithms differ greatly in implementation, and they use separate procedures for calculating and managing the curve shape and the curve evolution.

4.1 Framework

This section presents the representation and implementation of deformable models used in the proposed algorithm. An in-depth description of this framework can be found in [10].

4.1.1 Curve representation

The active contour is represented as an equidistant set of nodes along the curve. The curve-point coordinates are sub-pixel resolved and are resampled after each iteration using linear interpolation. Since the algorithm does not include forces in-between nodes in the deformation process, the curve representation use a variation of the finite difference method.

4.1.2 Curve deformation

The previous segmentation algorithm[10] use a modified Euler-Lagrange equation which states that the force equilibrium criteria must only be satisfied in the local normal vectors along the curve:

$$\hat{n} \cdot \hat{F}_{ext} - \hat{n} \cdot \hat{F}_{int} = 0 \tag{4.1}$$

Where $\hat{n}$ is the curve normal and the resulting forces are the projection of $\hat{F}_{ext}$ and $\hat{F}_{int}$ on the curve normal. This modification makes the forces effect the relative node positions of the curve to a lesser extent, which allows less amount of equidistant node resampling to be used compared to models with unconstrained node movement [10, 9]. The curve evolution is controlled by an iterative process, in which the curve evolution depend on the normal direction along the curve, the forces and a scaling factor c:

$$\gamma_{l+1}(s) = \gamma_l(s) + c(\hat{n}F_{ext} - \hat{n}F_{int})\hat{n} \tag{4.2}$$

The scaling factor is calculated as the product of a constant times the smallest node distance, divided by the largest net-force for the whole curve. The external force consist of a weighted sum of one regional statistics-based force F_R and an edge force F_E. The internal force F_{int} consist of a weighted sum of a curvature force F_C, a temporal acceleration force F_M and a temporal damping force F_D. F_E and F_R are the only forces which are described in detail in this report, since they are the only forces from the previously published framework that are used in the proposed vessel segmentation algorithm. An in-depth description of all the forces can be found in [10].

4.1.3 Regional statistics based forces

The region-based force of a node at time frame t is calculated from the corresponding coordinate in a so called probability map of the image. The probability map is derived from the magnitude image, and the pixel intensities of this map ranges from -1 to 1 (Eq 4.3). A negative probability map intensity at a node coordinate will result in a compressing region force in the normal direction of the node, and a positive balloon image intensity will result in an expanding force in the opposite normal direction. The probability map is based on two distinct Gaussian distributions, G_v and G_{nv} which represents vessel probability and non vessel probability, respectively. The distributions are calculated with the EM algorithm [8], which take regional magnitude-intensities, from an area assumed to contain both the vessel to be segmented and non vessel tissue, as input. The two distributions are then combined into a region-probability function, $R(I)$ according to (Eq. 4.3 - 4.5). This function converts the intensities of the magnitude images $I(x, y)$ into pixel probabilities in the probability map, $I_R(x, y)$. An example of a probability map is shown in Figure 4.1

$$I_R(x, y) \in [-1, 1] \tag{4.3}$$

$$R : [0, 1] \rightarrow [-1, 1] \tag{4.4}$$

$$R(I(x, y)) = \left\{ \begin{array}{c} \min(G_{nv}), \text{ when } I(x, y) < E[G_{nv}] \\ G_v - G_{nv}, \text{ when } E[G_{nv}] < I(x, y) < E[G_v] \\ \max(G_v), \text{ when } E[G_v] < I(x, y) \end{array} \right\} \tag{4.5}$$

4.1.4 Edge forces

The edge detector in use is implemented as several small directional sensitive filters for smoothing and differentiation of the magnitude image. The filters are oriented in four evenly spaced directions ($\phi = 0°, 45°, 90°, 135°$) within half of the unit circle, and the output of the detector is four different edge images $E_i,\ i = 1, ...4$ for each direction. The filter kernels are all one-dimensional in the sense that the 0 degree kernels are single-row vectors, and the directional sensitivity is achieved by rotating the filter kernels. Since the image grid is oriented along the x and y directions, the spatial resolution of rotation is not isotropic for all four rotation angles. The impact of this effect can be reduced significantly if smoothing filters are applied to the image prior to the edge-detection. The pre-smoothing of an edge image is performed **a** times in the direction of the selected edge-filter kernel, and **b** times perpendicular to the edge-filter kernel, where **a** and **b** are the parameters used to control the amount of smoothing. The 0 degree differentiation kernel is implemented as the second order differentiation filter **f** (Eq. 4.6), while the smoothing filter **s** is shown in (Eq. 4.7). Even though far more advanced and optimized edge and smoothing filters exist, the use of small

filter kernels have the advantage of efficient computation.

$$f = [-1\ 2\ -1] \tag{4.6}$$
$$s = [1\ 2\ 1]/4 \tag{4.7}$$

The edge force at a curve-node coordinate x is determined by the corresponding pixels in two edge-images E_l, E_{sl} selected by the algorithm. The edge selection chooses the two images in the set, with filter directions $\hat{e}_l, \hat{e}_{sl}$ closest to the curve normal ($\max(|\hat{n}\hat{e}|)$). The information from the two edge-images are combined according to (Eq. 4.8). The direction selective edge-force allows the algorithm to only consider *apriori* estimated edge directions, which enables the possibility to disregard spurious edges. Finally the edge force F_E can be expressed as:

$$F_E(s,t) = \hat{n}\frac{|\hat{n}\hat{e}_l|E_l(s,t) + |\hat{n}\hat{e}_{sl}|E_{sl}(s,t)}{|\hat{n}\hat{e}_l| + |\hat{n}\hat{e}_{sl}|} \tag{4.8}$$
$$|e_l| = |e_{sl}| = 1 \tag{4.9}$$

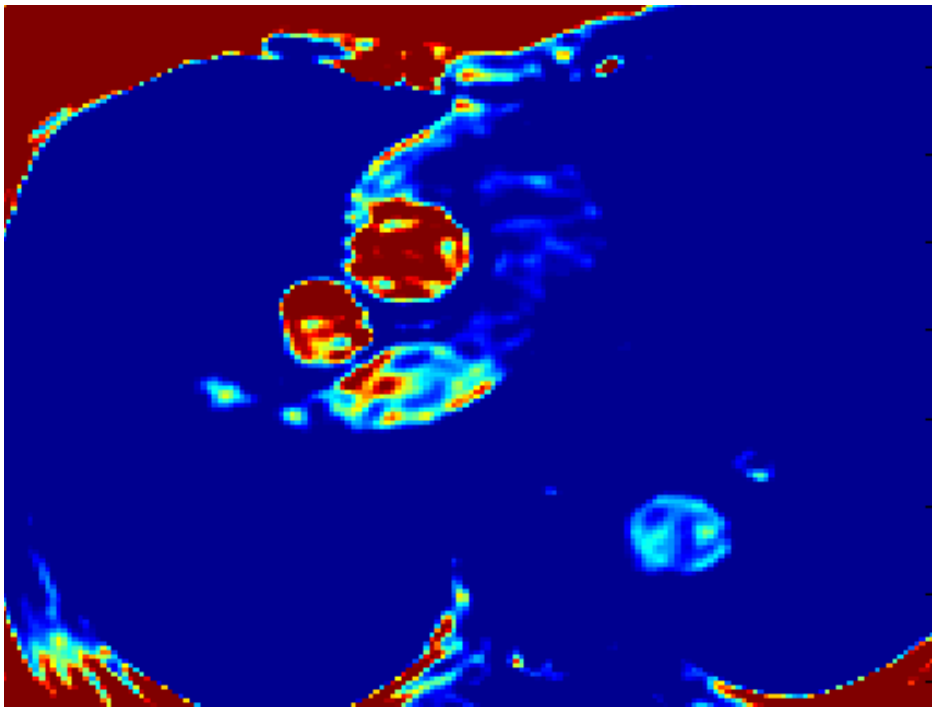

Figure 4.1: Example probability map for the vessel inside the large red circular shape in the image center. Red/yellow pixels result in an expansion force, while blue/green pixels result in compression.

4.2 Proposed vessel segmentation algorithm

The vessel segmentation problem can be described as the task of finding the actual contour of a relatively rigid, moving object at all available time frames. The object also has to contain considerable amounts of detected blood-flow during a heart-cycle. Considering the mentioned conditions, the following assumptions were made:

1. Vessel movement: The algorithm should account for movement of the vessel mass-center during a heart cycle and movement between two time frames is assumed to be limited.
2. Vessel shape: The vessel is expected to expand and compress itself to some extent, while conserving its initial geometrical shape throughout the sequence.
3. Blood-flow: The flow profile of the vessel has a detectable systolic peak, resulting from ventricular contraction, and near-homogeneous/laminar flow is expected in atleast one time frame.
4. Visibility: The vessel should be distinguishable from surrounding anatomical structures in the majority of time frames. Specifically in the form of pronounced edges and/or regional intensity changes.

The proposed deformable model use the edge force F_E and a modified version of the region-based force F_R from (Section 4.1.3) as external forces and the internal force consist of a single customized spring force F_S, which seek to preserve the initial shape and size of the contour. These forces together with the assumptions above make out the basis of the segmentation approach. The limited vessel movement assumption (1) allow the algorithm to initialize the contour at each time frame as the segmentation result of a previously processed, adjacent time frame. Furthermore, the area and shape constraints followed by assumption (2) are taken into account by using the custom springforce F_S, more specifically by including snake-area constraints into F_S. Assumption (3) is implemented as a second part of F_R, where regional information from the phase image (velocity information) is used, and finally, assumption (4) motivates using the magnitude image (Anatomical information) as the primary source of external information.

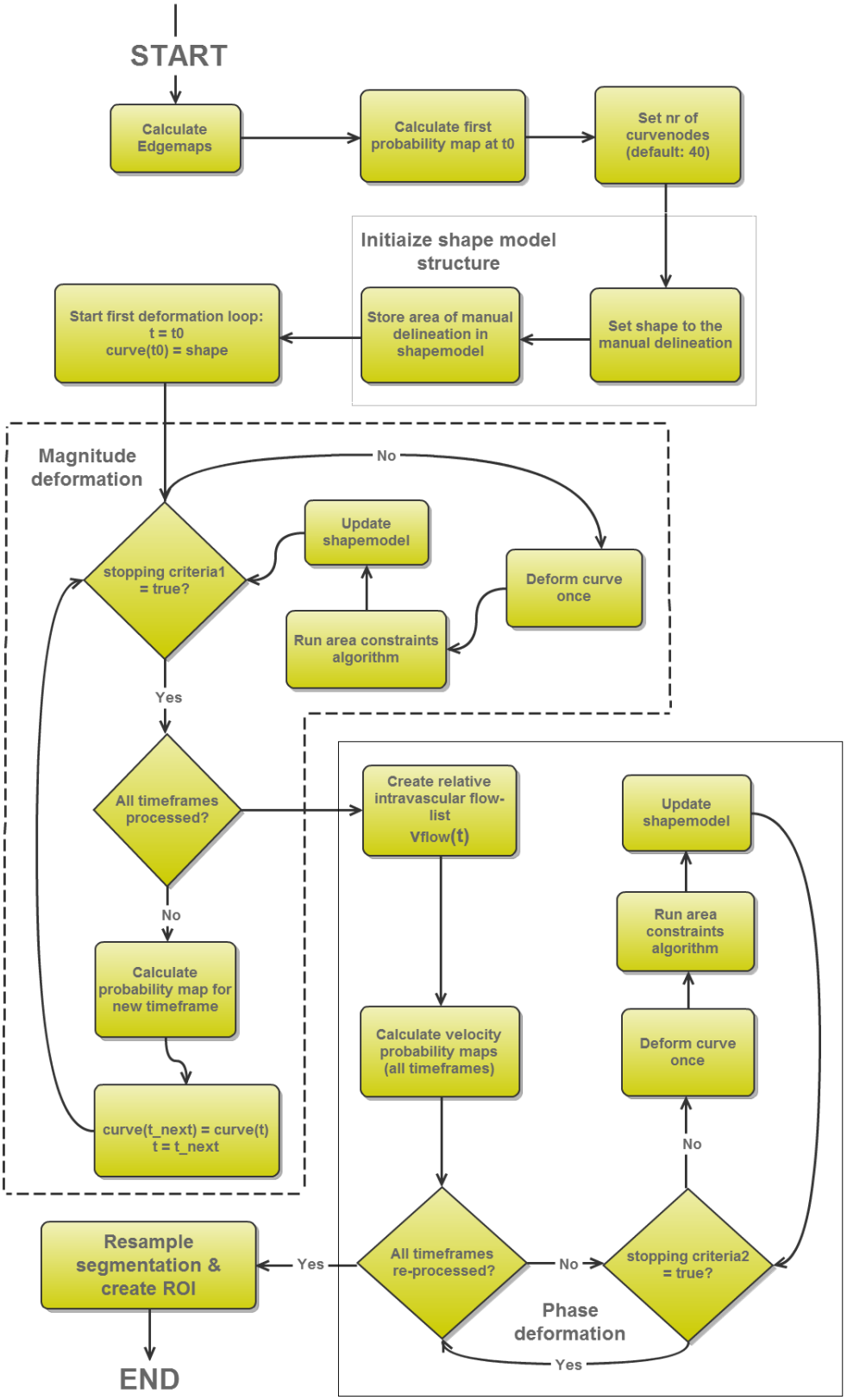

Figure 4.2: Flow-chart of all steps in the algorithm.

4.2.1 Algorithm structure

A complete flow-chart of the algorithm is found in Figure 4.2. The deformable curve is initialized in one time frame t_0 from a manual vessel delineation by the user. This serves as the shape basis for the spring force F_S and the first regional statistics used in F_R (for t_0) are calculated using all pixel values inside the manual delineation region of the magnitude image. The order of which different time frames are processed is centred around t_0, due to the time frame processing of the algorithm followed by assumption (1), and t_0 is further assumed to contain the most accurate estimation of the vessel boundary. As seen in the flowchart, the algorithm starts with the calculation of the edgemaps (from the magnitude image) used in F_E for the entire dataset (see Section 4.1.4 for details). It then proceeds by calculating the region based probability map used in F_R from the magnitude image in time frame t_0.

Regional-based force F_R

The region based force F_R use the same framework and statistical estimation algorithm (EM-estimation for gaussian mixtures [8]) as the region-based force described in Section 4.1.3. It is, however, modified to handle the added challenges of tracking a moving vessel. Compared to the relatively stationary center of mass for the left ventricle, the center of mass for the main arteries are changing over time and the pixel intensity distributions inside a vessel varies during the course of a heart-cycle, with a significant vessel intensity peak in mid-systole and a minimum mean in diastole, where (in some cases) vessel intensities are almost identical to that of the surrounding tissue. Therefore, it is not very likely to get an accurate and reliable region-analysis in all time frames.

The EM algorithm[8] is initialized with a first guess classification of the pixels inside a chosen analysis window. Care must be taken in selecting the size of this analysis window, since a small window might only contain vessel tissue, and a large window could include a third tissue class, such as lung tissue, which has a considerably lower intensity mean than the rest of the image, which very well might result in a classification where all non-lung tissue is grouped together in a single class. The manual delineation in t_0 is assumed to be the most accurate estimation of the vessel shape, and since the vessel compression/expansion is further assumed to be limited, the analysis window is chosen as an expanded version of the manual delineation ROI from t_0, shifted to the updated mass center of the deformable curve in the current time frame. The ROI expansion is set to 1.5.

The first guess classification is performed by calculating a likely vessel-intensity threshold and then assigning all pixel intensities above that threshold to the vessel class. The rest of the pixels inside the analysis window is assumed to belong to the non-vessel class. The threshold is obtained by calculating the mean and standard deviation (SD) for a set of pixels inside the analysis window, which most likely belongs to the vessel class. This pixel subset is chosen as all pixels inside a compressed version of the analysis window with a scaling factor of (1/3). The process of generating a probability map from the output of the EM algorithm[8] is identical to the process described in Section 4.1.3.

However, the effective direction of the used region-based force F_R differ slightly from the one previously defined in Section 4.1.3. Instead of using the curve normal as the primary force-direction, a normalized angular vector between the node point (y, x) and the mass center (y_M, x_M) serves as the direction of deformation. This was changed due to the occurrence of curve-loops in the proposed algorithm when applying F_R along the curve normals.

Shape model and the spring force F_S

The shape model at time frame t_0, $S(t_0)$ is initialized with the users manual delineation (see flowchart). Additionally, the inner area of the manual delineation is calculated and used as reference for the area constraint algorithm.

The purpose of the spring force is to prevent the node points of the curve to drift too far from the shape model. The force consist of a shape node/curve node distance check ($|(y_S - y, x_S - x)|$) and a conditional force calculation (Eq. 4.10-4.14). If a curve node is positioned within a predefined distance, called spring-slack (sl in Eq. 4.12 and 4.14), from its corresponding shape model node, the spring force is calculated as the product of a weight coefficient w, and an attenuation function $\dot{a}_n(\dot{v})$ (Eq. 4.12). The spring force act in the direction towards the shape model node ($\dot{v}$ in Eq. 4.11) and if a curve node moves outside the spring-slack distance sl, it will be pulled back completely to its corresponding shape model node (second row of Eq. 4.12). In order to enable deformation of the curve, curve nodes have to be allowed to deviate somewhat from the shape model (assumption (1)). Thus the spring-slack parameter sl has to be set to a positive, non-zero value (default unit is mm). However, a too large spring-slack may change the general shape of the curve, due to extensive deformation. The attenuation function ($\dot{a}(\dot{v})$) returns a vector in the direction of $\dot{v}$, which amplitude increase non-linearly (squared) with the curve node/shape node distance. In comparison with a corresponding linear function, the non-linearity result in a smaller deformation penalty (spring force) for small curve node/shape node distances (Eq. 4.14).

$$w \in [0, 1] \tag{4.10}$$

$$\dot{v} = (y_S - y, x_S - x) \tag{4.11}$$

$$\dot{F}_S = \begin{Bmatrix} w \cdot \dot{a}(\dot{v}), \text{ when} |\dot{v}| < sl \\ \dot{v}, \text{ when } |\dot{v}| > sl \end{Bmatrix} \tag{4.12}$$

$$(y_{new}, x_{new}) = (y, x) + \dot{F}_S \tag{4.13}$$

$$\dot{a}(\dot{v}) = (|\dot{v}|/sl)^2 \cdot \dot{v} \tag{4.14}$$

In contrast to the external forces, the spring force is applied after the deformation of the curve nodes is completed. This allows the spring force to act directly on the deformation of the current iteration. Since it is not included in the net force sum (Eq. 4.1), the effect of the spring force is independent of the explicit size of the external forces. The new node positions are derived in (Eq. 4.13).

$$G = \underset{g \in \Re}{\arg\min} \, ||g \cdot X_{shape} - X_{curve}||_2 \tag{4.15}$$

In order to satisfy assumption (2), the algorithm has to allow a united expansion/compression of the entire curve within a manually set area constraint parameter, the so called area-slack. The expansion/compression behaviour is implemented as a rescaling of the initial shape model, $S(t)$, at the end of each iteration, after the spring force have been applied to the deformable curve. The rescaling is performed by multiplying the shape model coordinates with an optimized scaling factor G (Eq. 4.15). It is defined as the value g which minimizes the L_2 norm of the curve node/shape node distance showed in (Eq.4.15), an optimization problem which can be solved analytically. The resulting shape model, $S(t)$, is shifted to be centred around the mass center c of the current deformable curve, and interpolated to match the angular position of the curve nodes. The area constraint function calculates the relative area difference between the rescaled and the original shape model. If the rescaling algorithm

result in an area change larger than the area-slack, the shape model is changed back into the original, unscaled shape model, centred around a custom mass center c_i so that the nodes responsible for the unwanted expansion/compression is exposed to the largest spring force (see Figure 4.3).

The custom mass center algorithm traverse along the nodes of the deformable curve to find local mass centres. At a specified number of curve nodes the curve normal is calculated, and the node directly opposite the current one, with respect to the curve normal, is found(see Fig 4.4). The opposite node is found by calculating the difference vector for the current node and all other nodes on the curve and then choosing the difference vector with the largest projection onto the curve normal. The custom mass center is calculated as the mean position of the two opposite nodes and two adjacent nodes on each side. The result is a mass center which only takes a small part of the curve into consideration and therefore, will only be affected by local shape deviations. Local expansions/compressions of the curve outside the limited node set is thus ignored. Since the algorithm calculates several custom mass centres, one has to be chosen. The mass center that results in a shape model region which includes the most pixels from the real vessel of interest is selected. This is evaluated by matching the pixels in each shape model candidate with the corresponding pixels of the segmentation result from the previous timeframe, and by calculating the flow content inside the shape model candidate from the phase image. This assumes a preservation of the spatial distribution of pixel intensities between adjacent timeframes and that the vessel of interest contain the majority of flow in the local vicinity.

The shape rescaling and the mass center shifting of the shape model is disabled for the time frame in which the area constraints have been exceeded. This prevents additional expansion/compression of the deformable curve. The rescaling and mass center shifting is re-enabled upon processing of the next time frame.

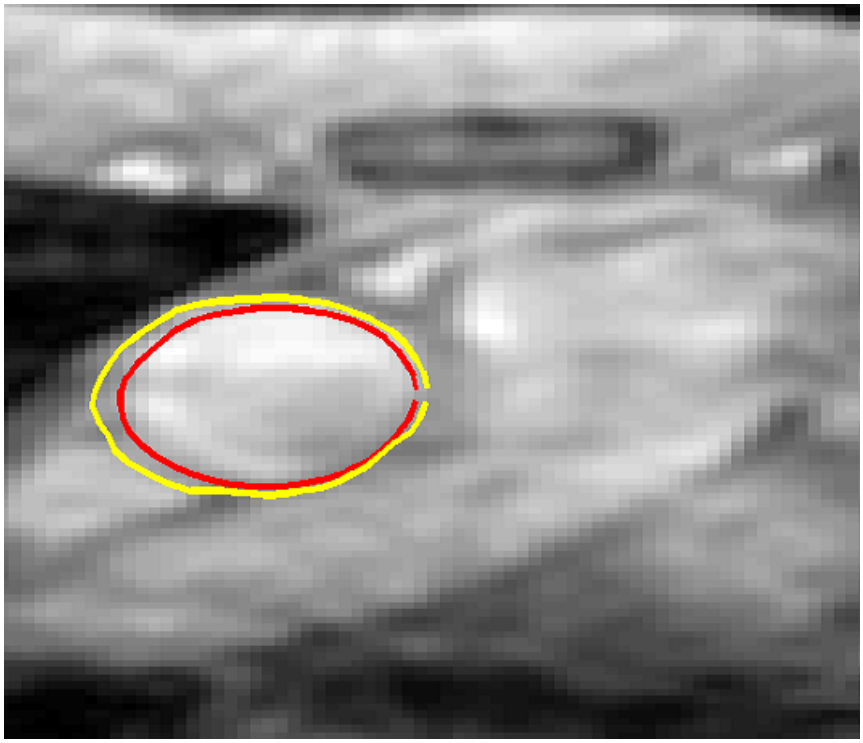

Figure 4.3: The shape model (in red) is centered around a custom mass center in order to maximize pullback of the expanding nodes. Due to the unwanted curve expansion, the regular mass center of the deformable curve (in yellow) is shifted away from the actual vessel.

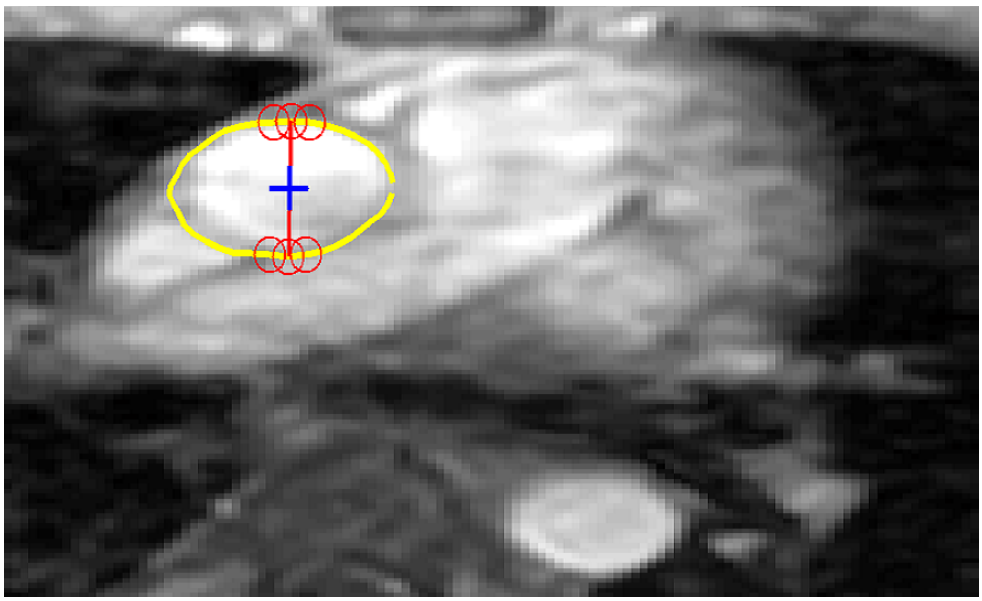

Figure 4.4: The custom mass center (blue cross) is calculated as the mean position of the marked curve nodes (red circles). The red line indicates the difference vector corresponding to the largest projection on the curve normal, while the deformable curve is shown in yellow.

First deformation loop

After the initialization of the shape model, the algorithm enters the deformation loop and the first deformation of the curve (in t_0) is performed. The springforce, shape model and the the stopping criteria are all updated after each deform iteration, while the probability map used in F_R remains unchanged in the current timeframe.

The stopping criteria for the first deformation loop is shown in (Eq. 4.19). The deformation change between each iteration is defined as the size of the unshared regions (Eq.4.17) of the enclosed curve areas of two consecutive iterations $(l, l-1)$. The region inside a closed curve $\gamma_l(x, y, t)$, in timeframe t, is represented by the binary mask $A_l(x, y, t)$ in (Eq. 4.16). The unshared region area $\Delta Area$ (Eq. 4.18) is divided by the area of the manual delineation $Area_{ref}$ to make the stopping criteria independent of absolute area sizes. When the relative area of the unshared region ($\Delta Area/Area_{ref}$) decrease beneath a set value (α in Eq. 4.19), the stopping criteria is fulfilled and the deformation process for the current timeframe is stopped. If the stopping criteria remains inactive, the deformations will automatically stop after a specified number of iterations (default is 30). When the deformation of a timeframe is complete, the region based probability map for the next timeframe is calculated, a stage in which the algorithm makes use of the updated centre of mass of the deformable curve. In addition, the curve initialisation of the next timeframe is set as the current segmentation result before the new deformation start. This process is repeated until all timeframes have been processed.

$$A_l(x, y, t) = \begin{Bmatrix} 1, \text{ inside } \gamma_l(x, y, t) \\ 0, \text{ outside } \gamma_l(x, y, t) \end{Bmatrix} \tag{4.16}$$

$$\Delta A_l(x, y, t) = (A_l(x, y, t) \cup A_{l-1}(x, y, t)) \cap \neg(A_l(x, y, t) \cap A_{l-1}(x, y, t)); \tag{4.17}$$

$$\Delta Area_l = \int\int_D \Delta A_l(x, y, t) dx dy; \tag{4.18}$$

$$stop\ criteria: \ (\frac{\Delta Area_l}{Area_{ref}} < \alpha), \text{ while } l \leq 30; \tag{4.19}$$

The segmentation is refined with the velocity information in the phase images in order to increase inclusion of significant flow. This velocity analysis is implemented as a second run of the deformation algorithm, with only the springforce F_S and the region based force F_R activated. A velocity-based probability map R_v is calculated from the phase images to be used in the new region based force F_R.

Velocity based probability map

Since, significant flow is only present in a limited number of time frames during systole, the velocity information in itself does not contain enough information for reliable and robust region-analysis of the entire dataset, and the specific time frames in which significant flow is present in the vessel of interest are not known *a priori*. However, by using the deformed curve derived from the magnitude image, an estimation of the total flow of the vessel in all time frames could be conducted. The total flow includes both positive and negative velocities and is thus defined as the absolute value of each pixel in the unbiased velocity image (pixel intensities centred around zero). The resulting flow values are normalized and stored in $v_{flow}(t)$ (Eq. 4.22).

The velocity probability map R_v is defined as the absolute value of all pixels in the unbiased

velocity image (the total flow map), weighted by the normalized flow in $v_{flow}(t)$ (Eq. 4.22). The idea is that all significant velocities should result in an expansion of the deformable curve in order to improve the algorithms inclusion of flow. Since a velocity image rarely contain pixels with strict zero values, all pixels in the image will result in an expanding region based force F_R. However, the systolic time frames are assumed to contain high velocity content inside the vessels compared to the surrounding tissue. This will lead to a discontinuity in the amplitude of the expansion force F_R. The stopping criteria for the velocity based deformation should be designed to detect and activate on such discontinuities. The temporal weighting with the normalized flow $v_{flow}(t)$ result in an unattenuated region based force F_R (normal expansion) in the time frame with maximum flow, and highly attenuated F_R (weak expansion) in the diastolic time frames (with low intravascular flow). A well designed stopping criteria should activate after only a few iterations in diastolic time frames to prevent large expansions for unsignificant flow. For this purpose, the relative flow measure could be included in the stopping criteria to distinguish systolic/diastolic time frames.

$$I_v(x,y,t) \in [-0.5, 0.5] \tag{4.20}$$

$$|I_v(x,y,t)| = \left\{ \begin{matrix} I_v(x,y,t),\ I_v(x,y,t) > 0; \\ -I_v(x,y,t),\ I_v(x,y,t) < 0; \end{matrix} \right\} \tag{4.21}$$

$$v_{flow}(t) = v_{tot}(t)/v_{totmax}; \tag{4.22}$$

$$R_v(x,y,t) \in [-1, 1]; \tag{4.23}$$

$$R_v(x,y,t) = v_{flow}(t) \cdot |I_v(x,y,t)|; \tag{4.24}$$

Second deformation loop

The second deformation loop use the rescaled shape models from each time frame from the first deformation as shape models. The deformable curve is initialized in each time frame as the segmentation result from the previous deformation and the processing of time frames are no longer centred around t_0, since no information from the refining deformation needs to be shared between time frames.

The stopping criteria for the second deformation run is modified to handle the new behaviour of the velocity based region force F_R. Since the new probability maps result in curve expansions of variable degree in all pixels, the stopping criteria must be able to recognize a significant decline in curve deformation between iterations caused by the snake traversing across a systolic flow boundary(see Section 4.2.2). It also has to feature variable sensitivity for systolic/diastolic time frames in order to prevent extensive curve expansion in time frames with low intravascular flow. The modified stopping criteria is shown in (Eq. 4.28). While the measure for deformation and the automatic iteration stop (default is 30) are reused (Eq. 4.19), the algorithm waits for five iterations before any evaluation of the stopping criteria is performed. It then use the maximum deformation value (Eq 4.25) as reference in order to capture significant deformation decline. The stopping criteria is considered to be fulfilled if the deformation measure between the latest consecutive iterations decrease below a set fraction ϵ of the reference value (Eq. 4.27). This fraction is weighted with the relative intravascular flow $v_{flow}(t)$ (Eq. 4.26) for each time frame in order to create variable stopping sensitivity (Eq. 4.28). After the second deformation of the curve, the segmentation is finally

resampled and stored as a new ROI in the selected image sequence.

$$Ref = max(\frac{\Delta Area_L}{Area_{ref}}),\ L = 1, ..., 5; \tag{4.25}$$

$$w(t) = v_{flow}(t); \tag{4.26}$$

$$\alpha(t) = w(t) \cdot (1 - \epsilon) \cdot Ref; \tag{4.27}$$

$$stop\ criteria:\ (Ref - \frac{\Delta Area_l}{Area_{ref}}) > \alpha(t),\ \text{while } l \leq 30; \tag{4.28}$$

4.3 Validation

The delineation result of the vessel segmentation algorithm was compared with manual delineations on a test set of 20 patients, a subset of a previous physiological study [1]. The comparison of detected stroke volume with manual delineation for each patient and the Dice coefficient [11] (Eq. 4.29) were used as performance measures for the algorithm. The inter-observer variability between manual delineation and the algorithm was also calculated as the difference in stroke volume between the two methods divided by the detected stroke volume of the manual delineation (gold standard), averaged over the test set. Although, the inter-observer variability in [1] was derived from cardiac index ($CI = \frac{\text{SV}\cdot\text{heart rate}}{\text{body surface area}}$) the two measures should be comparable since both observers/methods use the same values for heart rate and body surface area in each patient. The validation script was implemented as a plug-in into Segment, which made use of built in algorithms for flow calculations(reportflow.m), while a custom algorithm was developed to calculate the temporal mean of the Dice coefficient (Eq.4.29). The impact of chosen parameter values on the performance measures were estimated by calculating the averaged performance measures over all patients, and for several different values of springslack and areaslack respectively. The springslack and areaslack were estimated as the most critical parameters during development and testing and neither are described in the literature. The Dice coefficient measure d was calculated as:

$$d = \frac{1}{T}\sum_{t=1}^{T}\frac{2 \cdot (V(t) \cap M(t))}{V(t) \cup M(t) + V(t) \cap M(t)}; \tag{4.29}$$

Where $V(t)$ and $M(t)$ represents the region inside the automatic/manual segmentation, in time frame t, respectively.

Chapter 5

Results

This chapter presents statistical data and segmentation examples from the proposed algorithm. The result of the validation process is followed by brief illustrations of typical segmentation behaviour.

5.1 Parameters

Table 5.1: Effect of different parameter values with/without the second deformation loop

springslack [mm]	areaslack	velocity deformation	Dice mean ± SD	SV bias ± SD [ml]	additional outliers
2	0.2	off	0.83 ± 0.14	-12.30 ± 18.11	+2
3	0.2	off	0.87 ± 0.06	-8.62 ± 7.63	+1
6	0.2	off	0.86 ± 0.10	-9.80 ± 13.57	+1
20	0.2	off	0.88 ± 0.03	-7.03 ± 3.42	0
10	0.2	off	0.88 ± 0.03	-6.69 ± 3.22	0
10	0.4	off	0.85 ± 0.10	-9.89 ± 12.11	+1
10	0.8	off	0.81 ± 0.15	-11.76 ± 10.15	+2
10	1.0	off	0.78 ± 0.16	-13.12 ± 10.01	+3
10	0.01	off	0.88 ± 0.02	-7.57 ± 4.36	0
10	0.10	off	0.88 ± 0.02	-7.01 ± 2.92	0
2	0.2	on	0.83 ± 0.14	-9.94 ± 18.92	+2
3	0.2	on	0.87 ± 0.06	-5.97 ± 7.38	+1
6	0.2	on	0.86 ± 0.10	-7.08 ± 13.40	+1
20	0.2	on	0.89 ± 0.03	-4.36 ± 3.06	0
10	0.2	on	0.89 ± 0.02	-4.01 ± 3.03	0
10	0.4	on	0.86 ± 0.11	-7.28 ± 11.84	+1
10	0.8	on	0.82 ± 0.15	-9.11 ± 9.79	+2
10	1.0	on	0.78 ± 0.16	-10.50 ± 9.82	+3
10	0.01	on	0.89 ± 0.02	-5.00 ± 3.75	0
10	0.10	on	0.89 ± 0.02	-4.39 ± 2.58	0

Table 5.2: Interobserver variability vs Auto-Manual variability

	springslack	areaslack	velocity deformation	variability ± SD
Manual-Manual	-	-	-	3 ± 4 %
Auto-Manual	10mm	0.10	Yes	6 ± 3.6 %

The validation was performed with 10 variations of the areaslack and springslack parameters as shown in Table 5.1, with and without the second velocity-based deformation loop. For all tested parameter values, one outlier in the patient set was constantly present. In order to obtain quantitative meaningful information this outlier was excluded from Table 5.1 (for details, see Section 5.3). In Table 5.1, the Dice measure and the Stroke Volume bias between manual segmentation and the proposed method, averaged over the 19 included patients, were used as main performance measures. The presence of additional outliers were also noted (rightmost column). According to these measures, the performance of the algorithm is highly dependent on the selected parameter values and additional outliers were present for large values of areaslack or small values of springslack. The velocity deformation loop resulted in a decreased stroke volume bias for all tested parameter combinations. The largest mean of Dice coefficient of 0.89 and smallest SV bias of -4.01 ml was obtained with a springslack of 10 mm, an areaslack of 0.2 and with velocity information refinement. Additionally, the smallest standard deviation of the stroke volume bias was ± 2.58 ml and was obtained with a springslack of 10 mm, an areaslack of 0.1 and with velocity refinement. For comparison interobserver variability is shown in Table 5.2.

5.2 Performance plots

Three graphs showing the performance measures for each patient in the test set is shown in Figure 5.1 - 5.3. The spring/area-slack parameters were set to 10mm/0.2 respectively, with velocity refinement turned on. A bar diagram of the mean Dice coefficient for all patients is found in Figure 5.1. The dice temporal mean lies well above 0.80 for all patients except for the mentioned outlier in Section 5.1 (Patient nr.1, marked with red in the figure).

The detected stroke volumes from manual delineation and automatic segmentation (the proposed algorithm) are shown in Figure 5.2, together with a the linear regression and the identity line. Here, the outlier from Section 5.1 was excluded. In the majority of patients, the proposed algorithm results in underestimation of stroke volume. The blood volumes of the patients stay relatively close to the linear regression. The difference in measured blood volume between the two methods are shown with the Bland-Altman plot [12] in Figure 5.3. The data (all patients except the outlier from Section 5.1) features a negatively biased mean of -4.02 ml, with a standard deviation of ± 3.03 ml.

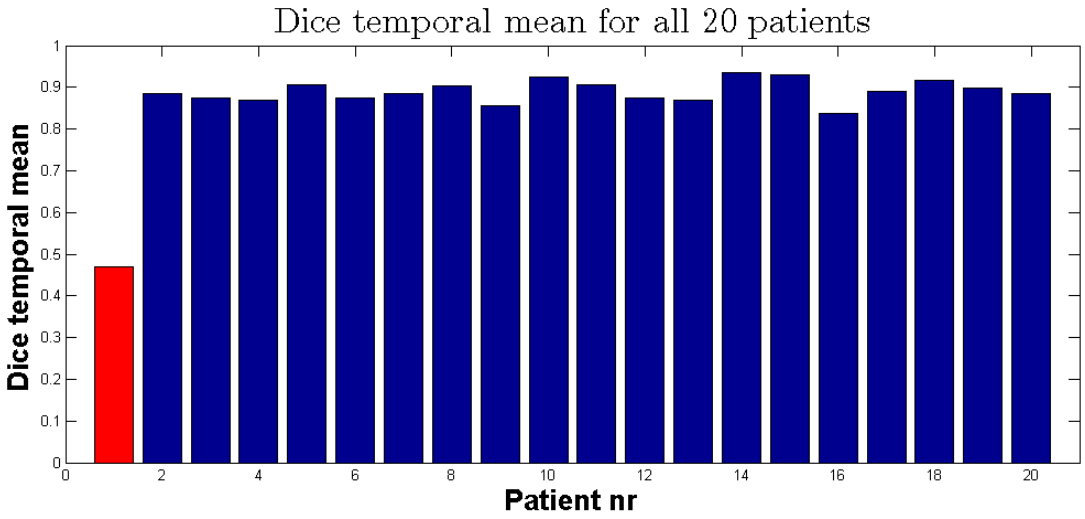

Figure 5.1: Dice temporal mean for each patient (bar). The outlier is marked with a red bar.

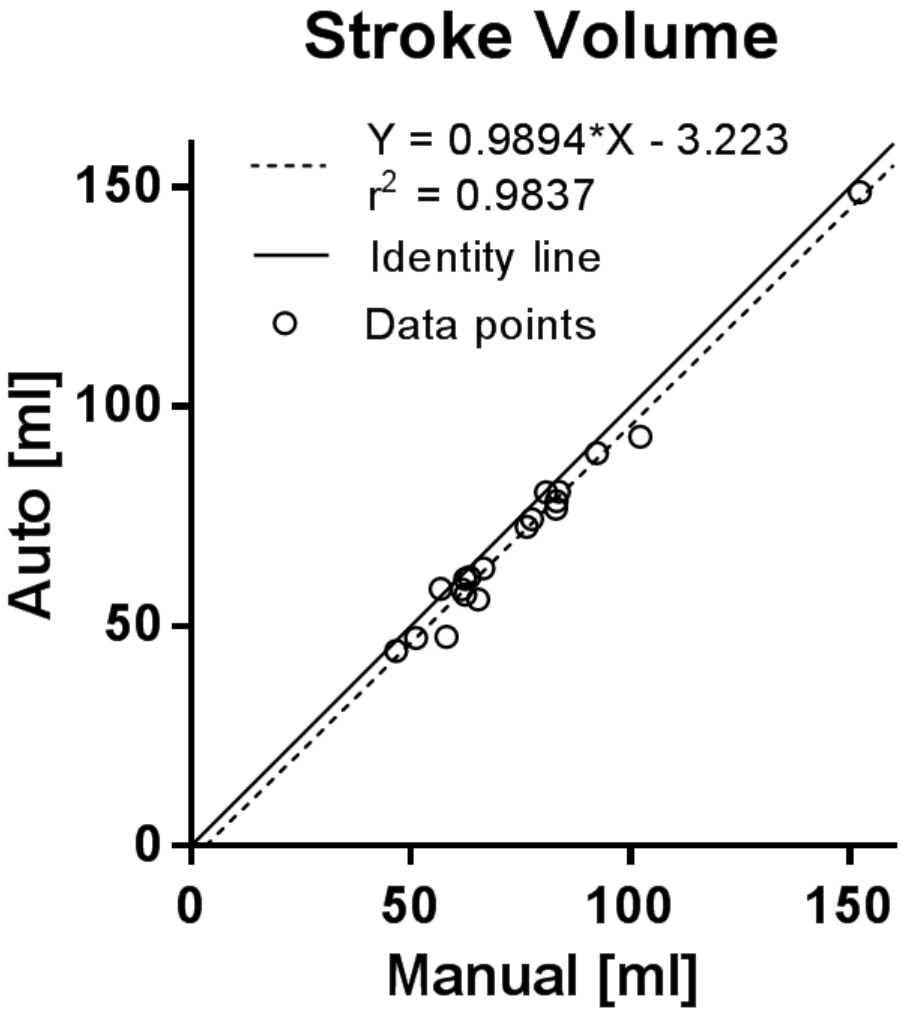

Figure 5.2: Stroke volume of manual delineation vs the proposed algorithm. All patients are included in the linear regression except for the outlier.

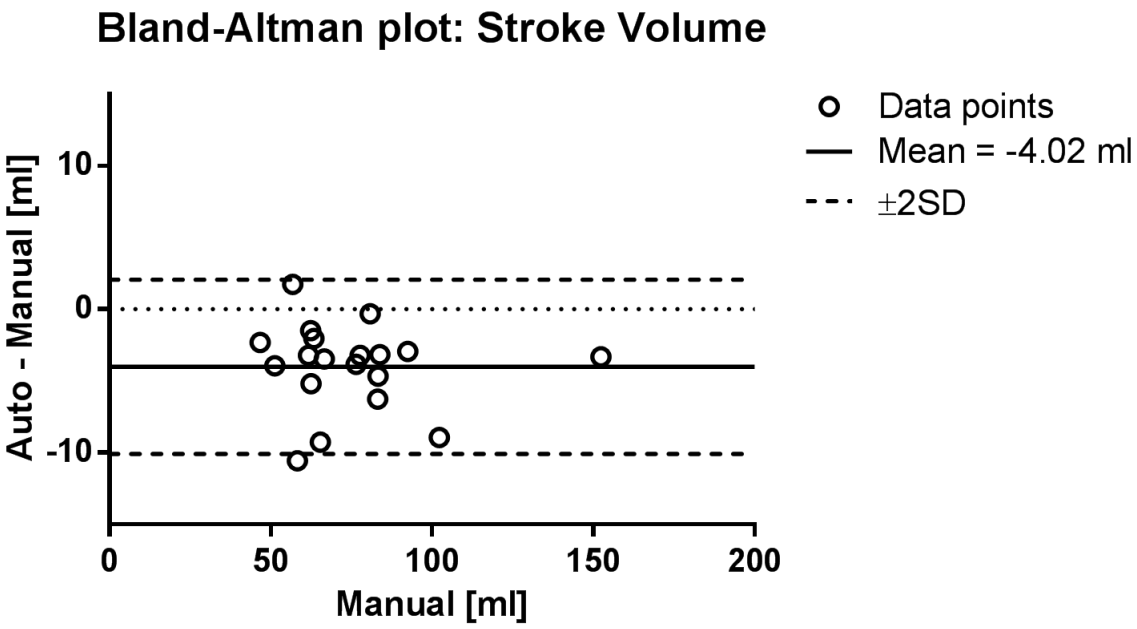

Figure 5.3: Bland-Altman plot of measured stroke volume. The negative bias is clearly visible in this graph (solid line).

5.3 Segmentation behaviour

Two screenshots from a segmentation result of the proposed algorithm in mid systole/diastole respectively, are shown in Figure 5.4. The accurate systolic segmentation and the diastolic underestimation of the vessel is seen frequently throughout the testset.

A screenshot from the failed segmentation from the outlier (red bar in Figure 5.1) is shown in Figure 5.5 and one of the inaccurate probability maps is shown in Figure 5.6. The outlier distinguish itself from the other patients in the test set by a high temporal resolution, where the majority of time frames does not feature a vessel intensity distribution mean which differs significantly from the surrounding tissue.

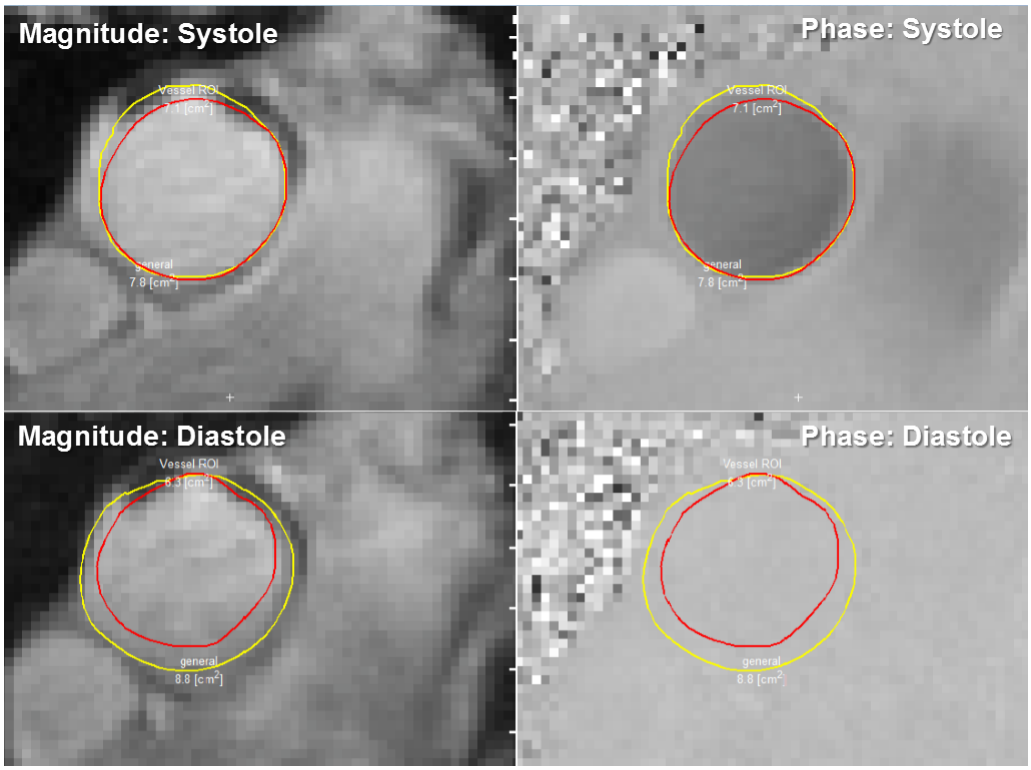

Figure 5.4: Magnitude/Phase image pair showing typical behaviour of the proposed algorithm in mid-systole (top row) and mid-diastole (bottom row). The manual delineation is marked with yellow while the deformable curve is coloured in red.

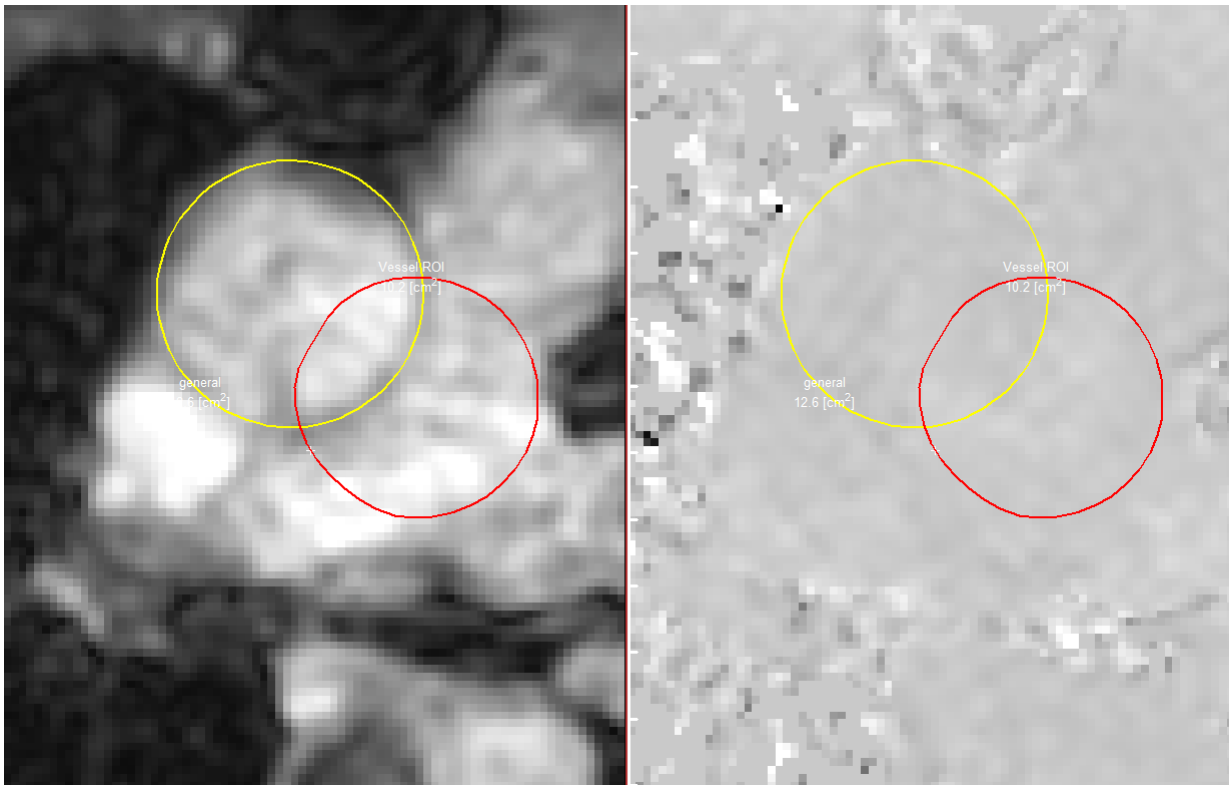

Figure 5.5: Magnitude/Phase image pair of the failed segmentation of Patient nr.1. The deformable curve (red circle) diverges from the manual delineation (yellow circle) in time frames where the region analysis fails to detect the vessel boundary, and little to no velocity information is available (right image).

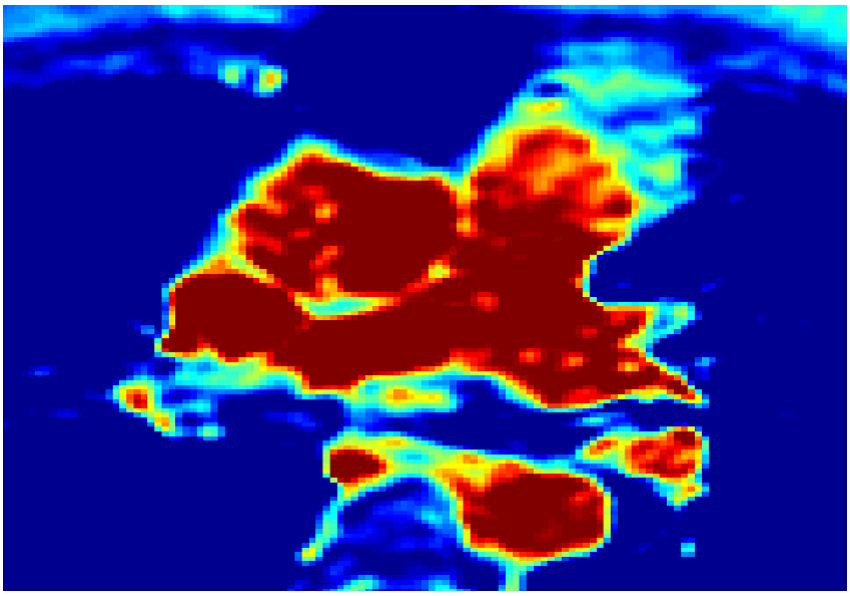

Figure 5.6: One of the probability maps of the failed segmentation (Patient nr.1). Blue/green pixels result in compression while red/yellow pixels result in expansion. The vessels are not separated by a compressing boundary and most non-lung tissue is assigned to the vessel class (red/yellow pixels).

Chapter 6

Conclusion and Discussion

This thesis suggests an automated method for vessel segmentation based on a previously developed deformable model framework. The main features are shape and area constraints, together with usage of velocity data for curve refinement.

Validation of the method indicates that the proposed, automated algorithm agrees well with the gold standard (manual delineation). There was a slight underestimation (bias) of stroke volume in all patients, and for all tested combinations of parameter values. When velocity information was not used, the negative bias increased, showing that the velocity information improves the segmentation to some extent. The automatic segmentation exhibit unstable behaviour when exposed to long image sequences without a clear distinction between the vessel and background, seen in one of the patients. In this case, the region-based probability maps were not able to distinguish the vessel of interest from its surroundings and the deformable curve moved freely within the area with similar pixel distribution in the magnitude image, as seen in Figure 5.5. This behaviour may originate from the strong temporal dependencies imposed by the algorithm, or the absence of temporal smoothing. In a final implementation the algorithm should be improved to handle such difficulties.

Adjustments of two key parameters indicate that a high degree of freedom, in the form of large springslack, tends to improve performance. However, further testing with a larger dataset is necessary before any conclusions regarding optimal parameter values can be made. Since performance of the algorithm is sustained for a significant decrease of the area-slack parameter, one could conclude that the segmentation result relies on the area constraint algorithm to a larger extent. This was not expected, since the area constraints were designed to handle instabilities associated with failed regional analysis in a limited amount of timeframes. Additionally, the large freedom of the custom mass center algorithm may cause significant curve movement between timeframes. Even though such behaviour increase the flexibility of the algorithm, it is a source of instability and should not be considered a robust method for vessel tracking. Another major drawback of the presented method is that it does not use any *a priori* information regarding vessel movement or realistic expansion/compression. Despite these limitations, the variability between manual segmentation and the proposed method is comparable with the inter-observer variability found in [1].

Future development of the algorithm can be done in several areas. First of all, temporal smoothing or temporal dampening should be implemented to improve robustness. Second, the stopping criteria for both deformation loops should be validated thoroughly in order to

improve detection of convergence. An alternative approach would be to represent the method as an energy minimization problem and thereby converting all the forces to sources of energy, where all timeframes are deformed in each iteration. Such a representation enables the area and shape constraints to be formulated as two independent sources of energy. Furthermore, statistical data of real vessel behaviour could be gathered and used to implement prediction based algorithms into the segmentation framework. These improvements will be explored in an upcoming project by the cardiac MR group.

In conclusion, the developed algorithm shows potential by performing close to the inter-observer variability, but improvements in robustness and stability is needed before it can be considered for clinical use.

Bibliography

[1] M. Carlsson, R. Andersson, K. Markenroth, K. Steding, H. Mosen, F. Stahlberg, B Ekmehag, and H. Arheden. "Cardiac output and cardiac index measured with cardiovascular magnetic resonance in healthy subjects, elite athletes and patients with congestive heart failure.". *Journal of Cardiovascular Magnetic Resonance*, 14(51), 2012.

[2] Cardiovascular diseases "http://www.who.int/mediacentre/factsheets/fs317/en/index.html". *Fact sheet Nr. 317*, 2012.

[3] C Kramer, J Barkhausen, S Flamm, R Kim, and E Nagel. Standardized cardiovascular magnetic resonance imaging (CMR) protocols, society for cardiovascular magnetic resonance: board of trustees task force on standardized protocols. *Journal of Cardiovascular Magnetic Resonance*, 10(35), 2008.

[4] H. Arheden, M. Bajc, M. Carlsson, F. Hansen, B. Jonson, K. Bloch, O. Pahlm, J. Petterson, I. Rosen, E. Johansson, H. Westling, B. Wohlfart, P. Wollmer, and S. Andersson. *Klinisk fysiologi med nuklearmedicin och klinisk fysiologi*. Liber, 2011. ISBN978-91-47-09931-3.

[5] P. R. Moran. A flow velocity zeugmatographic interlace for NMR imaging in humans. *Magnetic Resonance Imaging*, 1(4):197–203, 1982.

[6] N. J. Pelc, F. G. Sommer, K. C. Li, T. J. Brosnan, R. J. Herfkens, and D. R. Enzmann. Quantitative magnetic resonance flow imaging. *Magn Reson Q*, 10(3):125–47, 1994.

[7] E. Heiberg, J. Sjogren, M. Ugander, M. Carlsson, H. Engblom, and H. Arheden. Design and validation of Segment–freely available software for cardiovascular image analysis. *BMC Med Imaging*, 10:1, 2010.

[8] M. Lorenzo-Valdes, G. I. Sanchez-Ortiz, A. G. Elkington, R. H. Mohiaddin, and D. Rueckert. Segmentation of 4D cardiac MR images using a probabilistic atlas and the EM algorithm. *Medical Image Analysis*, 8(3):255–65, 2004.

[9] D. Kucera and R. W. Martin. Segmentation of sequences of echocardiographic images using a simplified 3D active contour model with region-based external forces. *Computational Medical Imaging and Graphics*, 21(1):1–21, 1997.

[10] E Heiberg, L Wigström, M Carlsson, A Bolger, and M Karlsson. *"Time Resolved Three-dimensional Segmentation of the Left Ventricle in Multimodality Cardiac Imaging"*. PhD thesis. Linköping Studies in Science and Technology, 2004.

[11] L. R. Dice. Measures of the amount of ecologic association between species. *Ecology*, 26(3), 1945.

[12] J. Martin Bland and G. Douglas Altman. Statistical methods for assessing agreement between two methods of clinical measurent. *The Lancet*, February 8:307–310, 1986.